Exp Fluids (2011) 51:1139–1151
DOI 10.1007/s00348-011-1133-z

RESEARCH ARTICLE

Analysis of misfires in a direct injection engine using proper orthogonal decomposition

Hao Chen · David L. Reuss · Volker Sick

Received: 22 December 2010 / Revised: 25 May 2011 / Accepted: 26 May 2011 / Published online: 12 June 2011

Abstract Previous work demonstrated that the occasional misfired and partially burned cycles (MF) in a stratified-charge, spark-ignited direct injection engine always achieved an early flame kernel, but failed to reach and inflame the fuel in the bottom of the piston bowl. This conclusion was derived from intra-cycle crank angle resolved velocity and fuel concentration images that were recorded simultaneously using high-speed particle image velocimetry and planar laser-induced fluorescence. In this study, both ensemble average analysis, conditionally sampled on either MF or Well Burned (WB) cycles and proper orthogonal decomposition (POD) are applied separately to the velocity and fuel distributions. POD of the velocity and fuel distributions near the spark plug were performed, and the mode energy and structure of the modes are compared. This analysis is used to assess the similarity and differences between the MF and the WB cycles and to identify physical insight gained by POD. The POD modes were determined from the combined set of 200 WB and 37 MF cycles to create two sets of 237 orthogonal modes, one set for the velocity, V, and one for the equivalence ratio, ε. Then, conditionally sampled averages of the POD coefficients could be used to quantify the extent to which each mode contributed to the MFs. Also, the probability density functions of the coefficients quantified the cyclic variability of each mode's contribution. The application of proper orthogonal decomposition to velocity and equivalence ratio images was useful in identifying and analyzing the differences in flow and mixture conditions at the time of spark between well-burning and misfiring cycles. However, POD results alone were not sufficient to identify which of the cycles were misfiring cycles, and additional information was required for conditional sampling.

H. Chen · V. Sick
Shanghai Jiao Tong University, Shanghai, China

D. L. Reuss · V. Sick (✉)
The University of Michigan, Ann Arbor, MI, USA
e-mail: vsick@umich.edu

V. Sick
Center of Smart Interfaces, TU Darmstadt, Darmstadt, Germany

1 Introduction

Spray-guided spark-ignited direct injection (SG-SIDI) engines offer improved fuel economy by reducing pumping losses, which is realized by controlling the fuel that is injected into the cylinder rather than throttling the inlet mixture (Zhao et al. 1999). In order to create the ignitable mixture near the spark plug, the fuel spray is targeted at the spark plug for SG-SIDI engines. However, the close proximity of fuel spray and spark plug can create unfavorable flow and mixture conditions, which can lead to ignition failures (misfires) and partial burns (Fansler et al. 2008). Recently, the development of high-speed imaging diagnostics, which is also capable of simultaneously measuring velocity field and fuel concentration at crank angle resolution, has led to a better understanding of turbulent flow and fuel/air mixing and their role on ignition stability (Fajardo et al. 2006; Peterson et al. 2011; Peterson and Sick 2009; Sick et al. 2010a, b). Peterson et al. (2011) measured the velocity and equivalence ratio near the spark plug of an SG-SIDI engine idle operating condition where rare misfires and partial burns occurred. Results showed that the conditions during misfired and partially burned cycles were within the range seen for successful combustion. Further analysis showed that an ignition kernel was always formed, but that the equivalence ratio distribution was insufficient

for sustaining the flame. The leaning of the fuel path between spark plug and bottom of the bowl leads to partial burns or in extreme case, a misfire.

The present study provides further analysis of the data from Peterson et al. (Peterson et al. 2011), using two approaches to identify the causes which led to the poor mixture distributions. First, a more traditional approach, the velocity and equivalence ratio distributions are conditionally sampled to compute the mean of the well-burned cycles for comparison with the mean of the cycles, which misfired or partially burned. The second analysis employs the proper orthogonal decomposition, POD. The POD technique was introduced to turbulent flow by Lumley (Lumley 1967) as an objective means to extract coherent structures from a database of velocity fields. The goal of this analysis is to determine whether POD of the equivalence ratio and flow can provide more physical information than the traditional statistical analysis toward determining the causes of the unsuccessful fuel distributions.

2 Background

2.1 Summary of misfire and partial burn measurements from previous study

The data for this study are measurements made and fully described by Peterson et al. (Peterson et al. 2011). An SG-SIDI engine was operated at low-load 800-rpm idle condition. Optimal fuel injection timing was used with spark retarded one crank angle degree from optimum to produce rare misfired and partially burned cycles. Thirty-seven misfire and partially burned cycles of 4,524 total cycles were recorded during 13 different 348-cycle tests. The original study defined misfires as cycles where the indicated mean effective pressure (IMEP) was below zero and partially burns as cycles with positive IMEP, but a mass burned fraction of less than 0.5. For simplification of the discussion, we refer to all of these failing cycles as misfires (MF) and well-burned cycles are denoted WB.

The velocity and equivalence ratio distributions were measured near the spark plug using high-speed simultaneous particle image velocimetry (PIV) and planar laser-induced fluorescence (PLIF). The measurements were recorded simultaneously at each crank angle degree, during each injection-, spark-, and combustion-event, and for each consecutive cycle. Figure 1 shows Mie scattering images (upper row) of a well-burning cycle for five crank angles before ignition, as well as the superimposed velocity fields and equivalence ratio distributions for these five crank angles and three more images for crank angles after ignition. The crank angle scale is defined with CA = 0° at top dead center exhaust. The PIV and LIF laser sheets bisected the plane that included the fuel injector, the spark-plug gap, and the one of eight spray plumes that was targeted directly at the spark gap. The gas-phase flow momentum at the spark plug during and after the injection event is dominated by momentum transport from the liquid-spray and, thus, convected the spark plasma, the ignition kernel, and the partially premixed flame to the lower right of the pictures.

As shown by the Mie scattering images, the velocity and equivalence ratio distributions prior to 330° CA are dominated by the presence of the liquid spray. After 330° CA, the distributions have no measurements in the burned gases (regions bounded by the dotted line), due to the depletion of both the PIV oil-droplets and LIF biacetyl tracer by the flame (cf. Fig. 1). Thus, the analysis in this study focuses on CAD = 330°, which is the state of flow and fuel at the

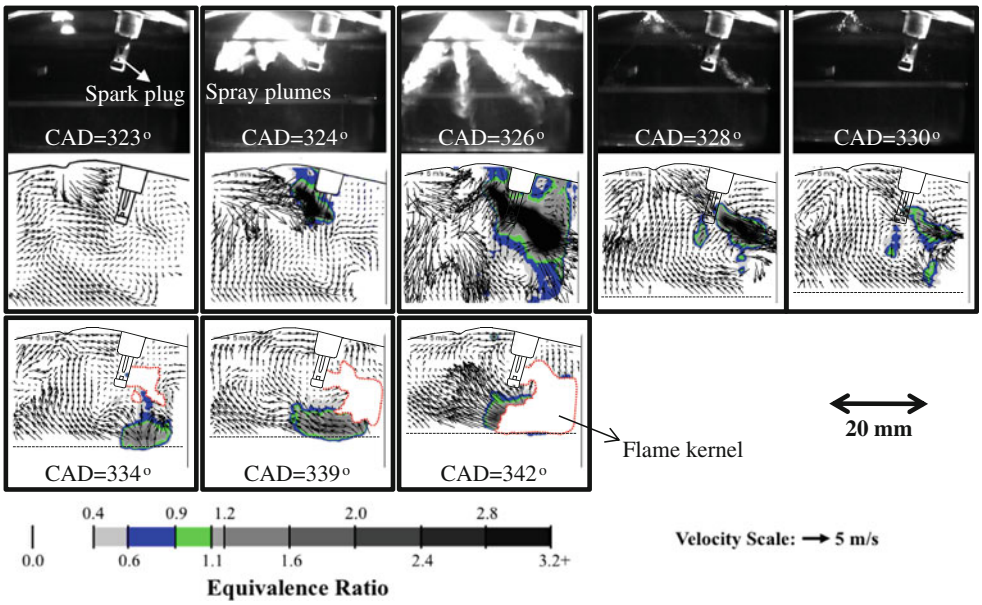

Fig. 1 Crank angle resolved Mie scattering images (*upper row*) and overlapped velocity fields and equivalence ratio image sequences from Peterson et al. (2011) (Fuel injection timing: 323°–328°ATDCExh, spark timing: 330°ATDCExh. Fuel equivalence ratio was measured only on right side of the combustion chamber)

beginning of the spark discharge. The gas-phase velocity measurements were taken over most of the field of view, but were unavailable where and when the spray was present. The LIF laser power was sufficient to illuminate only half the field of view and therefore was placed on the right half, where both the spark plasma and flame were convected. Figure 2a, b show the subregions of the velocity and equivalence ratio at CAD = 330°, respectively, which were analyzed in this study. These regions were defined to avoid image background features that would inject non-physical features into the POD analysis, which will be discussed in the next section.

The images in Fig. 1 show a well-burned cycle, where the early flame kernel (white area with red outline) at CAD = 334°, develops and propagates into the fuel cloud at the bottom of the piston bowl by CAD = 342°. Analysis of individual cycle PIV and PLIF images in Peterson et al. (Peterson et al. 2011) revealed that misfired cycles occur under lean mixtures and low velocities at the spark plug, but still within the range of values for the well-burned cycles. There was no correlation between the misfires and the spark-discharge energy, power, or duration. Observations of the fuel distribution and flame areas for the partial burns and misfires showed that an early flame kernel was always formed, but failed to develop sufficiently to propagate to the fuel in the bowl. A flame kernel arriving late within the piston bowl found significantly leaner conditions, and the mixture was not fully consumed leading to a partial burn. In misfire cycles, the mixture in the measurement plane was significantly leaner surrounding the flame kernel, which disappeared shortly after the spark discharge. That study concluded that the partial burns and misfires are not the result of failed ignition, but failure occurs during the flame propagation process.

2.2 Proper orthogonal decomposition analysis

Lumley proposed to use the POD technique to objectively extract coherent structures from turbulent flows (Lumley 1967). In engines, POD has been used for the analysis of cyclic variability of PIV measurements (Baby et al. 2002; Roudnitzky et al. 2006), proposed for low-order modeling of flows (Holmes et al. 1997), and used for comparison of flow measurements with LES computations (Liu and Haworth 2011; Sick et al. 2010b). It has also been used for the analysis of scalar and flame structures (Bizon et al. 2009, 2010). In this study, we apply phase-dependent POD to both the velocity and equivalence ratio measurements taken at a fixed crank angle degree, in an attempt to assess if it can provide physical understanding beyond that of ensemble averaging. The mathematical and conceptual principles of POD have been described at length in the literature (Chatterjee 2000; Cordier and Bergmann 2003; Holmes et al. 1996). Here, we describe only the properties of the POD decomposition that are salient to the analysis as we have applied it to the misfire study.

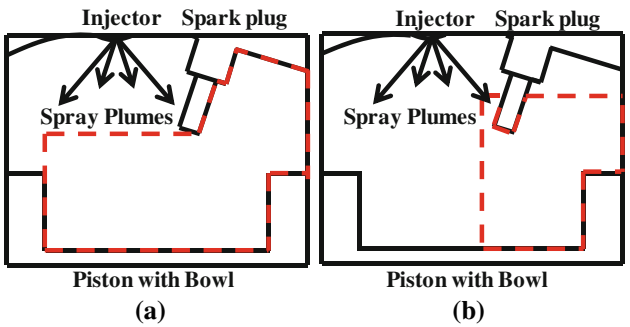

Fig. 2 Analysis fields of view in this study for (**a**) the velocity and (**b**) the equivalence ratio distributions indicated by the *red dashed lines*

In this study, we analyze the two-dimensional velocity, (u, v), distribution

$$V^{(k)} = (u, v)_{i,j}^{(k)} \tag{1}$$

and the equivalence ratio distribution

$$\varepsilon^{(k)} = (\varepsilon)_{i,j}^{(k)} \tag{2}$$

measured on a two-dimensional grid, (i, j), during each cycle, k, at one crank angle, for a total of K cycles (snapshots). The following description of the POD in Eqs. 3 through 9 is cast in terms of velocity. However, the equations apply identically to the equivalence ratio by replacing the two-dimensional velocity V with the one-dimensional scalar value ε.

Conceptually, the POD decomposes the original function $V^{(k)}$ into a linear combination of M spatial basis functions (POD modes, φ_m) multiplied with the corresponding coefficients $c_m^{(k)}$:

$$V^{(k)} = \sum_{m=1}^{M} c_m^{(k)} \varphi_m \tag{3}$$

where φ_m are M two-dimensional $(i \times j)$ normalized vector distributions. When the method of snapshots is used the number of created modes is equal to the number of cycles (snapshots) K (Sirovich 1987). Each basis function is orthogonal to all others and normalized (unity), so that $c_m^{(k)}$ determines the contribution of mode m to the reconstruction of the velocity $V^{(k)}$. The value of $c_m^{(k)}$ is determined by projecting $V^{(k)}$ onto the mth mode, φ_m. Thus, $c_m^{(k)}$ is an $M \times K$ coefficient matrix where there is one coefficient for each mode in each cycle. The values of $c_m^{(k)}$ can be positive or negative.

The procedures of determining the orthonormal POD basis functions φ_m are detailed in Holmes et al. (1996), Chatterjee (2000), and Cordier and Bergmann (2003) and

have been implemented for this work into a Matlab code to minimize the following function.

$$\sum_{k=1}^{K}\left\|V^{(k)}-\sum_{m=1}^{M}c_m^{(k)}\varphi_m\right\|^2\rightarrow\min \tag{4}$$

$$\text{subject to}\quad \left(\varphi_i,\varphi_j\right)=\delta_{ij}=\begin{cases}1 & \text{if } i=j\\ 0 & \text{if } i\neq j\end{cases}\quad\text{where}\quad \|\cdot\|$$

denotes the L^2 norm. Because of the use of the L^2 norm, it is natural to apply this to velocity distributions where $(c_m^{(k)})^2$ represents the kinetic energy the mth mode contributes in the kth cycle, though this physical interpretation is not appropriate in most cases where POD is used (Chatterjee 2000) and certainly will also not apply to our analysis of the equivalence ratio fields. Based on Eq. 3, the velocity field from a given cycle k can be reconstructed by summing all of the modes multiplied by their respective coefficient for that cycle. Likewise, the sum of the energy from all of the cycles captured by the mth mode is

$$e_m=\frac{1}{2}\sum_{k=1}^{K}\left(c_m^{(k)}\right)^2. \tag{5}$$

and the energy fraction of the mth mode is given by

$$E_m=e_m\Big/\sum_{m=1}^{M}e_m \tag{6}$$

The modes are ordered with decreasing corresponding energy such that the mode with $m = 1$ is the one with the highest energy.

The ensemble average of Eq. 3 will yield the averaged velocity fields as

$$\langle V\rangle=\frac{1}{K}\sum_{k=1}^{K}V^{(k)}=\sum_{m=1}^{M}\left[\frac{1}{K}\sum_{k=1}^{K}c_m^{(k)}\right]\varphi_m=\sum_{m=1}^{M}\langle c_m\rangle^K\varphi_m \tag{7}$$

and the contribution of each mode to the ensemble mean can be computed as

$$\langle V\rangle_m=\langle c_m\rangle^K\varphi_m \tag{8}$$

where the operator $\langle c_m\rangle^K$ indicates the ensemble average over all cycles for a given coefficient. The exact ensemble average is achieved when all modes are used and a lower-order estimate is achieved with a truncated set, e.g., for low-order modeling (Holmes et al. 1996, 1997).

POD is used frequently to identify coherent structures in measured data. Coherent structures are not necessarily completely captured by individual modes. However, when there are repeatable high-energy structures occurring in the same region of every cycle in an engine, such as in a pent-roof engine with symmetric intake ports, it is possible to capture most of the energy in a single mode with POD (Voisine et al. 2011). In this case, the coefficients capture the cycle-to-cycle variability of the energy in that single mode, which is estimating the structure. Liu and Haworth (Liu and Haworth 2011) applied POD for comparing computed and measured flow structures in an engine-like flow. The application of POD in this study is in the same spirit of these two studies, where we attempt to identify flow and equivalence ratio structures in the misfired and partially burned cycles that are not present in the well-burned cycles and could help to explain the reason for misfires.

Visual comparison of the modes, though useful, is both laborious and qualitative. Here, we use the "relevance index R_p" (Liu and Haworth 2011) obtained by projecting one basis function φ_a onto another basis function φ_b, to quantitatively measure the degree to which two basis functions from different samples are similar or dissimilar.

$$R_p=\frac{(\varphi_a,\varphi_b)}{\|\varphi_a\|\cdot\|\varphi_b\|} \tag{9}$$

The numerator denotes the inner product of two basis functions, and $\|\cdot\|$ denotes the L^2 norm. The numerical value of the relevance index varies from -1 to 1. $R_p = 1$ if the two basis functions are identical, $R_p = -1$ means two basis functions are exactly opposite, $R_p = 0$ if two basis functions are orthogonal. Of course, Eq. 9 can be used to quantify the similarity of any two velocity distributions as originally presented by Liu and Haworth (2011). Here, it is used to compare the mean velocity distributions with POD reconstructed distributions, as well as POD modes conditionally sampled on the WB versus MF cycles.

The above description has been in the context of the velocity where the minimization of Eq. 4 provides an intuitive energy-based decomposition. However, POD analysis has also been applied to image intensity for pattern recognition. For example, Sirovich et al. (Sirovich and Kirby 1987) used it for the "Rogue Gallery Problem", where it was utilized to identify one face out of a set of 115 faces. Thus, it is natural to apply this to flame features (Bizon et al. 2009, 2010) and other scalars measured in engines in a completely analogous way. In the present study, for the application to equivalence ratio distributions, the physical relevance of ε^2 is not as intuitive as the kinetic energy derived from the decomposition of velocity fields but nonetheless the POD modes are generated using the L^2 norm in Eq. 4. Thus, the equivalence ratio, ε, was substituted for V in Eqs. 3–8, and the modes were ordered by ε^2.

3 Results and discussions

The focus of this study is the analysis of flow and mixture conditions at the onset of spark, which were found before

as critical for successful ignition. First, we investigated the difference between WB and MF cycles by analyzing the conditionally sampled ensemble mean equivalence ratio and velocity fields. Then, the POD technique was utilized to identify additional physical information such as coherent flow features that contribute to the MFs.

The velocity and equivalence ratio distributions for over 4,000 cycles were recorded by Peterson et al. (Peterson et al. 2011). Those were all well-burning cycles with the exception of the 37 MF cycles analyzed here. However, we performed the ensemble mean and POD analysis for only 200 WB cycles for comparison with the 37 MF cycles to keep the computational effort at a level manageable with Matlab routines. We investigated the relevance of sample size and found that this was sufficient for an estimate of the mean and is also comparable with sample sizes used for POD analysis reported in the literature.

3.1 Conditionally sampled ensemble mean analysis

Figure 3a, b show the ensemble mean equivalence ratio conditionally sampled on the 200 WB cycles and 37 MF cycles, respectively. No differences are discernable in a visual comparison. However, their difference shown in Fig. 3c reveals that the well-burned cycles have locally richer regions around spark plug and leaner regions just downstream of the spark plug. The effect of sample size was investigated to show that these differences in Fig. 3c are not just statistical fluctuations. The ensemble mean of 200 WB cycles was subtracted from six ensemble averages of randomly selected 37-cycle WB samples. One of the subsamples with the largest differences is shown in Fig. 3d and illustrates the statistical validity of the sampling procedure. The maximum difference shown in Fig. 3c is over five times larger than those in the WB subsamples in Fig. 3d, strongly suggesting that the conditional samples indeed have different fuel distributions.

Figure 4 shows the same subtraction results for the velocity fields. Again, the subtractions between 200 WB cycles and subsamples do not show significant differences, indicating the effect of subsampling is small compared with the differences between the WB and the MF. There are two regions with vortical flow structures that only appear in the difference between WB and MF cycles. Those are highlighted in Fig. 4 by dotted and dashed circles. Most prominently, the difference vectors at the fuel spray tip (highlighted by the solid circle in Fig. 4a) have the opposite direction as the velocities caused by fuel spray. This demonstrates that the entrained gas velocity at the end of the liquid spray event (in the wake of the liquid jet) of the MF cycles is lower.

3.2 POD analysis

A POD analysis was performed to gain more physical insight into the differences between WB and MF cycles and also to examine whether a POD analysis could be used to identify MF cycles without prior knowledge that allows conditional sampling. In principle, conditional sampling could be performed at two stages of the POD analysis. First, the POD is performed on WB and MF data subsets separately, and then the modes and coefficients are compared. Second, POD is performed on the entire data set, and then the coefficients are conditionally sampled and analyzed. It is not a priori obvious which approach is more useful. Thus, both analysis approaches were taken, and results are reported here to illustrate that the second approach is more appropriate. Analyses of the equivalence ratio and velocity distributions are presented separately, followed by a comparison with the ensemble mean analysis.

3.2.1 POD of the equivalence ratio distributions, ε

The *first POD analysis* was performed on the equivalence ratio distributions, applied separately to the 200 WB cycles and the 37 MF cycles, thus creating 200 and 37 modes, respectively. It is implicit here that the 200 samples WB cycles are sufficient to capture the POD mode structures of the larger 4487 WB sample, which is consistent with samples sizes used in the literature, and large compared with the 37 available MF cycles produced by the

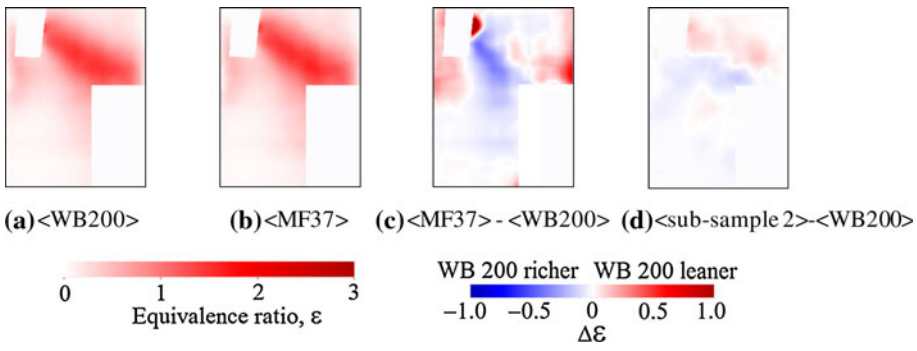

Fig. 3 Ensemble average equivalence ratio comparison, beginning of spark, CAD = 330°ATDCExh. ⟨·⟩ denotes the ensemble average. *Red regions* in **c** and **d** indicate leaner regions in the 200-cycle ensemble-averaged WB case; *blue regions* are richer

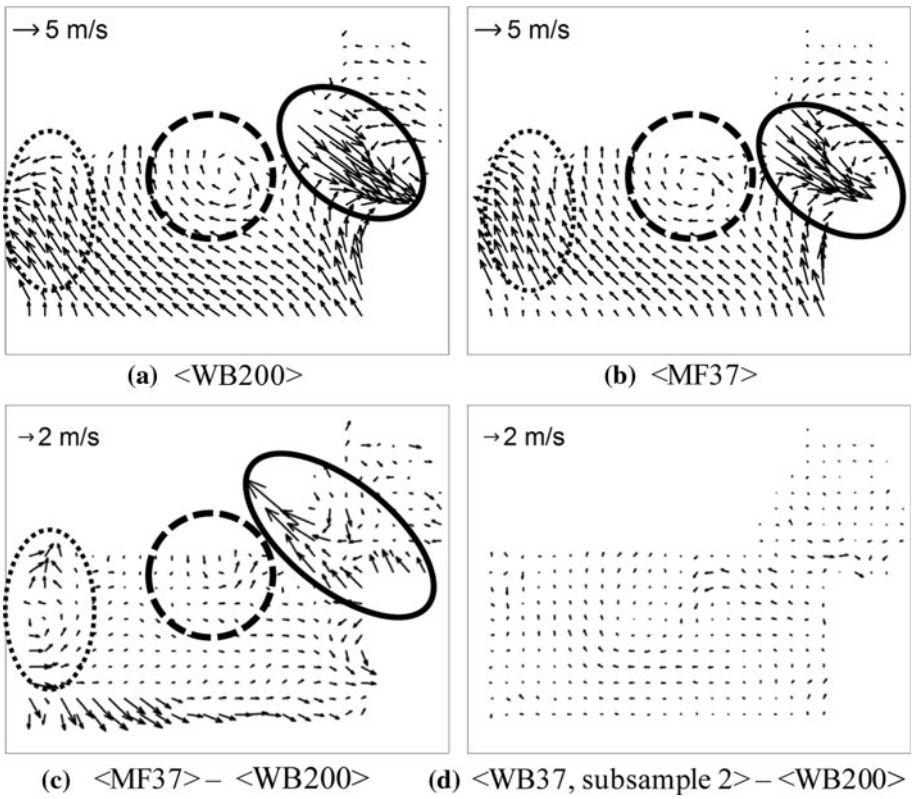

Fig. 4 The difference between conditionally sampled ensemble average velocity fields at the beginning of spark, CAD = 330°ATDCExh, shows the residual difference between WB and MF cycles. Flow structures in the highlighted regions are discussed in Sect. 3.3

experiments (refer to Sect. 2.1). To assess the effect of limited sample size, six subsamples of 37 randomly selected WB cycles were selected from the 200 WB cycles and analyzed with POD separately. Figure 5a shows that the six WB subsamples have essentially the same POD ε^2 spectra, but that mode 2 of the MF cycles is significantly higher in the ε^2 fraction. This difference between the MF and WB ε^2 fractions in Fig. 5a is significant only if the basis functions for the different spectra are the same. Since the basis functions are orthonormal with respect to the basis of each sample but not with respect to the basis functions of the other samples, it is necessary to quantify the equivalence of the mode patterns of the WB versus MF samples. R_p defined in Eq. 9 was employed to quantitatively measure the degree to which two modes from different samples are equivalent. Figure 5b shows six modes from one of the WB subsamples projected onto the first 20 of 200 modes generated from all 200 WB cycles. With the exception of R_p for mode 1, which is nearly equal to the mean, R_p is significantly less than unity for modes with the same sequence rank, which means that POD of the WB subsamples created modes that are significantly different from those for the full 200 WB cycle sample. This result could not be seen in the energy spectra that showed no significant difference between subsamples (Fig. 5a). Further, mode switching has occurred between the WB subsample and the full 200 WB sample. That is the mode order is based on ε^2 as shown in the spectra of Fig. 5a, but the maximum R_p of higher modes has switched order. This is particularly prominent for mode 9 of the subsample that correlates very well with mode 8 of the 200 WB samples. Modes 3 and 4 have not only switched order, but now correlate with some extend with adjacent modes. For completeness, Fig. 5c shows the maximum absolute value of R_p obtained by projecting modes of two of the 37 WB subsample modes and the MF modes onto the modes generated by all 200 WB cycles; this demonstrates that the modes of the subsamples do not correlate well with any of the higher modes of the full 200 WB cycles.

Taken together, Fig. 5a–c show two important results. First, the six WB subsamples have very similar mode spectra and mode correlations. However, R_p rapidly falls from unity ($R_p = 1$ for identical modes), which means that POD of the WB subsamples created modes that are significantly different from the full 200 WB cycle sample. Second, mode 2 of the MFs contributes more energy, but since R_p of the MFs shown in Fig. 5c is lower than that of the WB cycle samples, the coefficients (amplitude of the equivalence ratio contribution) of mode 2 of the WB cycles cannot be compared directly to the coefficients of mode 2 of the MF cycles. These two results illustrate an important property of the POD analysis. Namely that it is necessary to generate the POD modes from all 237 cycles (WB + MF) to guarantee that the same modes are generated for

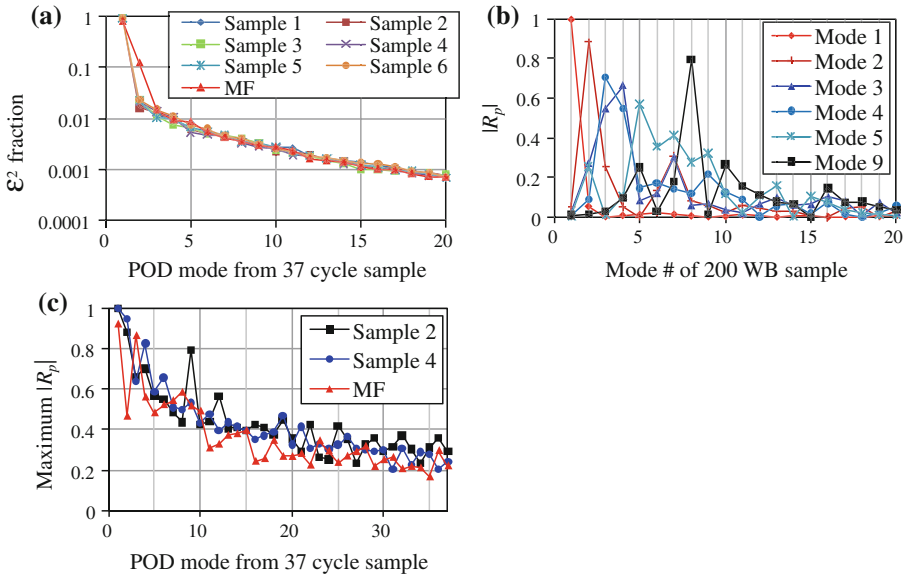

Fig. 5 **a** POD ε^2 spectra for six WB subsamples and the MF cycles; **b** the relevance index for six modes from a WB subsample projected onto the first 20 modes from all 200 WB cycles; **c** maximum correlation between each mode from three subsamples, two randomly selected 37-cycle WB subsamples and 37 MF cycles, projected onto all modes of the 200 WB cycles. CA = 330°

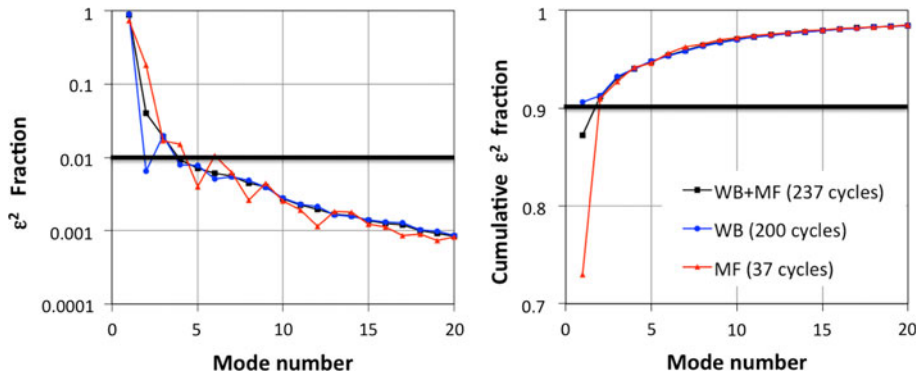

Fig. 6 POD mode spectrum of the ε^2 fraction (logarithmic scale) and cumulative ε^2 fraction (linear scale) for the first 20 POD modes of 237-cycle sample. The fraction is computed from the coefficients for WB + MF, WB, and MF, the basis functions for all three cases are same

meaningful quantitative comparison of the energy contained in the modes (i.e., comparison of POD coefficients).

The *second POD analysis* was applied to the equivalence ratio distributions from the 237 WB and MF cycles combined, thus producing a single set of modes and a single coefficient matrix. Then, conditional sampling of the matrix coefficients was performed. Figure 6 compares the POD mode spectrum of the ε^2 fraction and the cumulative ε^2 between the WB and MF cycles; only the first 20 of the 237 POD modes are shown. These values of ε^2 represent the summation of, $\left(c_m^{(k)}\right)^2$ (cf. Eq. 5), from all cycles (200 WB cycles, 37 MF cycles, and 237 WB + MF cycles, respectively) for each corresponding mode. Thus, the very high ε^2 for $m = 1$ of the WB cycles demonstrates that the equivalence ratio distribution is very repeatable. However, the considerably lower value for $m = 1$ of the MF cycles means that the higher modes contribute more to the conditionally averaged distribution. Nonetheless, the first five modes captured ~95% of the total ε^2 for all subsamples as shown in Fig. 6.

According to Eq. 7, the summation over all 237 modes multiplied with their respective coefficients will create the ensemble mean exactly. A low-order estimate is achieved by the first few modes (Fogleman et al. 2004, Holmes et al. 1997) and it was suggested that for this purpose two criteria be used. First, the cumulative energy, here ε^2, should be at least 90% of the total and second, all modes that contribute to at least 1% to the total should be included. For the present case, this includes modes up to $m = 5$. Figure 7 shows the reconstructed average equivalence ratio distributions that were obtained by conditionally sampling the coefficients before averaging them. The major difference between WB and MF cycles was captured by this low-order estimate; results agree with observations made from the ensemble-averaged images shown in Fig. 3 in that the equivalence ratio values are lower for MF cycles downstream of the spark plug.

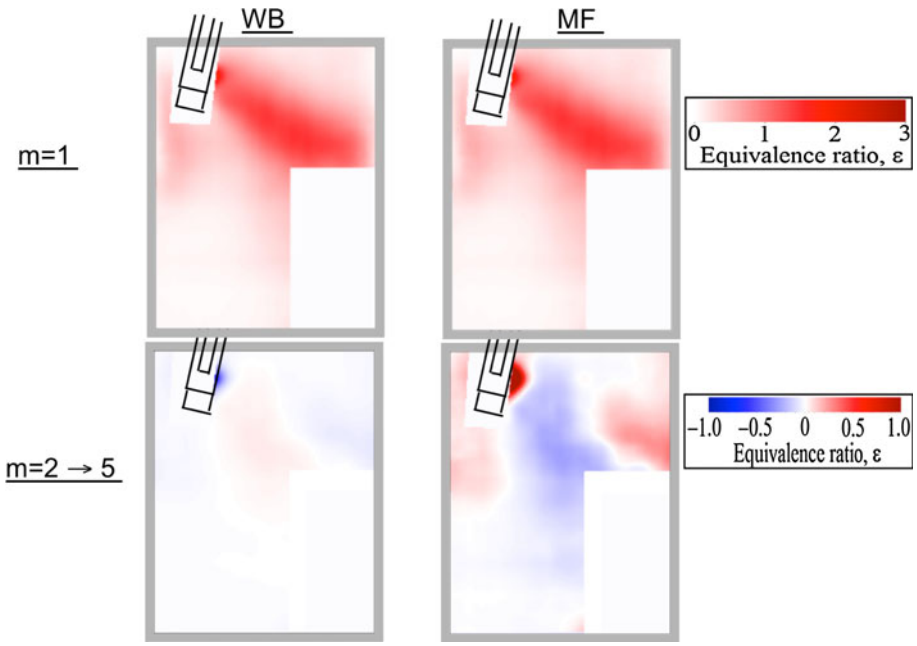

Fig. 7 POD analysis of equivalence ratio distribution from the decomposition of 237 WB and MF cycles combined and subsequent conditional sampling of the coefficients. The *upper images* show the contribution from mode 1. The lower distributions were obtained from the sum of modes 2–5 and clearly illustrate that their addition to the $m = 1$ fields will result in a leaner equivalence ratio for misfiring cycles downstream of the spark plug; compare with Fig. 3

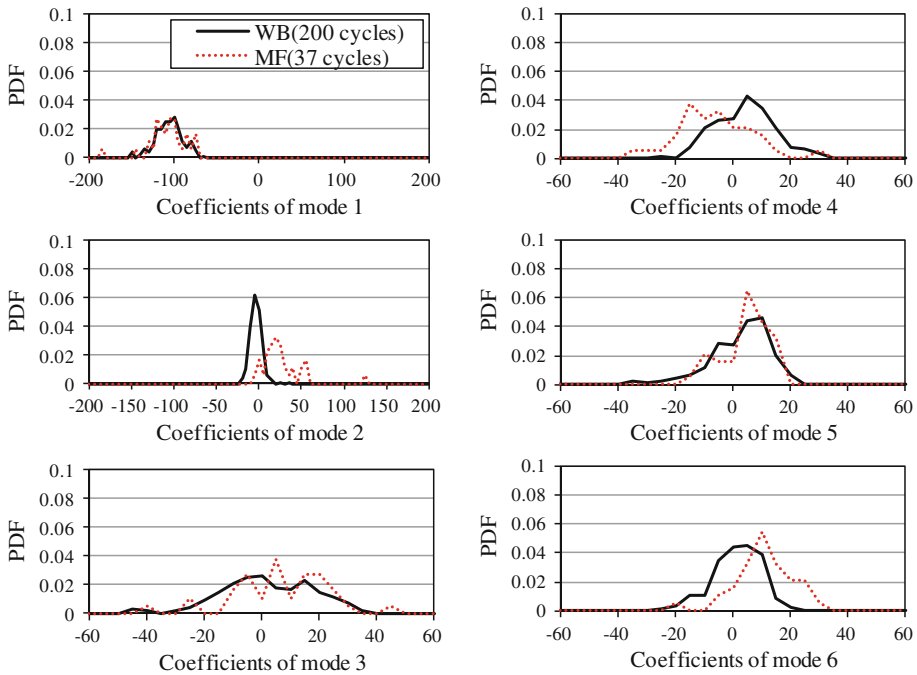

Fig. 8 Probability density function (PDF) of POD coefficients for Equivalence Ratio for WB and MF cycles. The coefficients were obtained from decomposition of all 237 WB and MF cycles

The difference between WB and MF cycles was captured with the contribution from a small number of modes only. The question arises whether an examination of the coefficients could reveal differences between WB and MF cycles without the need to invoke criteria used for the conditional sampling, i.e., IMEP in our case. Histograms of the coefficients for the first few modes are shown in Fig. 8. While there is a distinct shift for modes 2, 4, and 6, the distributions are not clearly separated and therefore could not be used to identify MF cycles from the POD analysis alone. Note that the 37-cycle sample size is too small to expect a smooth PDF; Fig. 8 serves only to quantify the range and cycle-to-cycle variability of the coefficients.

3.2.2 *POD of the velocity distributions*

In the same manner, as for the POD analysis of the equivalence ratio images, it was found that the POD

analysis of the velocity fields had to be performed on the entire data set. Then, conditional sampling of the coefficients and a consistent set of basis functions would better highlight the differences between WB and MF cycles. The square of the coefficients provides the kinetic energy according to Eqs. 5 and 6. Figure 9 shows the spectrum of the kinetic energy fraction and cumulative energy captured by the leading 20 POD modes for the WB + MF, WB, and MF cycles. Here, the energy fractions are based on the total energy of the respective conditionally sampled data set. As with the equivalence ratio analysis shown in Fig. 6, mode 1 had a higher energy fraction for the WB cycles than for MF cycles. It is also noteworthy that for the velocity data, the first 20 POD modes are required to capture approximately 90% of the total kinetic energy, compared with the equivalence ratio where the first mode alone captured 90% of ε^2 for the WB cycles. The same trend is followed for the other subsamples. As the first mode of the MF cycles has significantly lower energy than that of the WB cycles, many more of the higher-order modes are required to recover the same fraction of the total kinetic energy. According to the energy spectrum in Fig. 9, mode 4 in particular and modes 7 through 15 are more dominant in the MF cycles than the WB cycles.

The PDFs of the coefficients for the first four modes are shown in Fig. 10, illustrating the substantial cyclic variability of the coefficients. It is also evident that modes 1 and 4 have reversed roles between WB and MF cycles.

The conditionally sampled averaged flow fields were reconstructed, again employing the criteria that a lower-order estimate contain 90% of the total and neglect no modes with more than 1%. In contrast to the equivalence ratio distribution where 5 modes were sufficient for this, the velocity field reconstruction required the use of the first twenty modes. Figure 11 shows the reconstructed conditionally averaged flow fields and illustrates that for WB cycles the first mode captured the structure of the flow field whereas the reconstruction of the averaged MF cycle flow field shows the substantial modulation via contributions from modes 2–20. The point to be made here is that the *higher modes are not necessarily describing new or different coherent structures; in this case, they simply modulate the very repeatable mode 1 structures*. Summed together, the higher-order modes then quantify the total

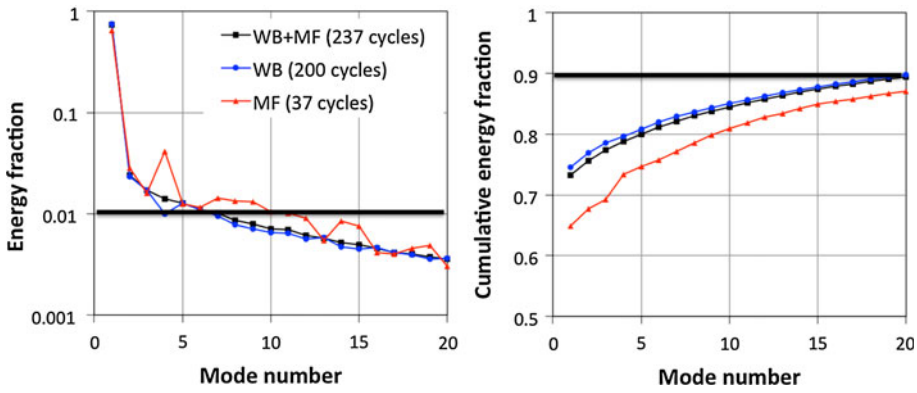

Fig. 9 Kinetic energy fraction (logarithmic scale) and cumulative energy fraction (linear scale) for the first 20 POD modes. The coefficients were obtained from a single decomposition of all 237 WB and MF cycles combined, but then were conditionally sampled

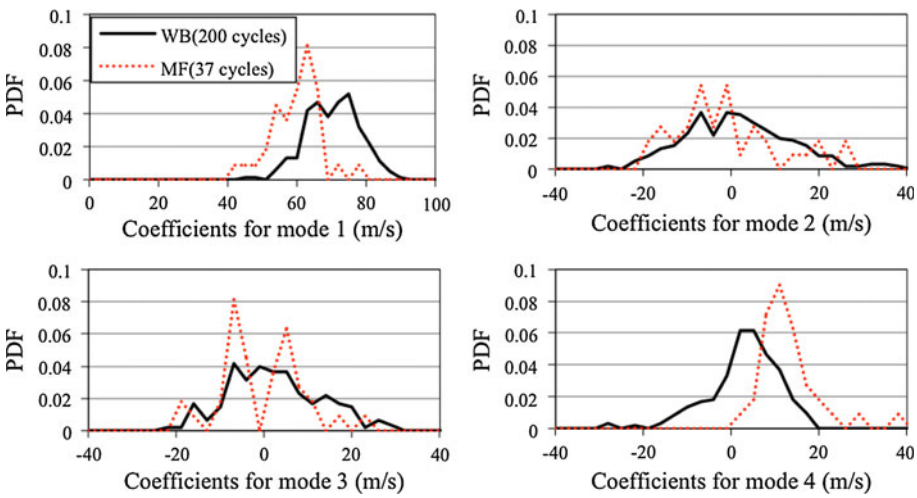

Fig. 10 Probability density function (PDF) of POD coefficients for velocity fields of WB and MF cycles. The coefficients were obtained from decomposition of all 237 WB and MF cycles

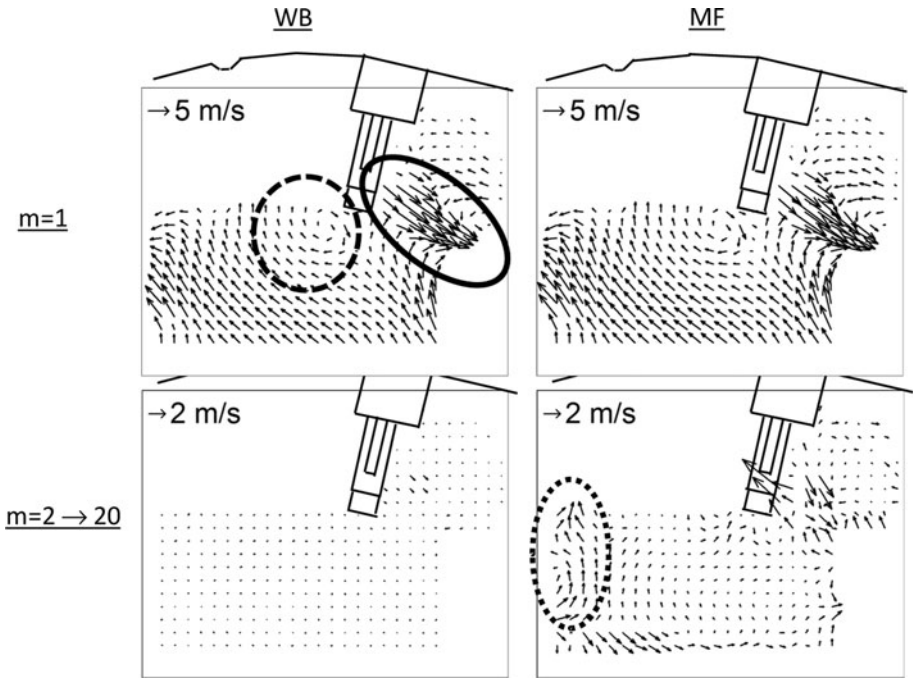

Fig. 11 POD analysis of velocity fields from the decomposition of 237 WB and MF cycles and subsequent conditional sampling of the coefficients. The *upper images* show the contribution from mode 1. The lower distributions were obtained from the sum of modes 2–20 and clearly illustrate that their addition to the $m = 1$ field will result in a lower velocity for misfiring cycles downstream of the spark plug; compare with Fig. 4. Features highlighted by circles are discussed below

modulation of the first mode. The cycle-to-cycle distribution of this modulation is revealed by the PDFs of Fig. 10 where the coefficients for MF mode 1 are smaller than for the WB values, but this is largely recaptured by the energy of MF mode 4.

The energy spectrum in Fig. 9 suggests that there is also more energy in the MF modes 5 through 15 compared with the same modes of the WB cycle modes. A summation including modes 2 through 20 (Fig. 11 lower right panel) shows that the resulting averaged flow field provides a reasonable estimate of the difference of the means (Fig. 4). This is reasonable, since mode 1 is a good estimate of the mean (high-energy fraction) and was excluded from the summation here, effectively subtracting the mean.

3.3 Discussion of ensemble mean versus POD analysis

The main motivation for this study was to determine whether POD analysis could provide more physical insight into the causes of the MFs that was not accessible through ensemble averaging and whether POD could be used to identify MF cycles without the use of conditional sampling based on indicated mean effective pressure and mass burned fraction. Here, conditional sampling was employed prior to ensemble averaging velocity and equivalence ratio images to then compare results of the WB cycles versus those of the MF cycles. Ensemble averaging V or ε structures in a reciprocating engine is ambiguous because it is unknown if the average distribution exists in every cycle or if the average is dominated by but a few cycles with large magnitudes. POD could remove this ambiguity. Recall that both averaging and POD analyses were performed for images that were captured downstream and adjacent to the spark plug at 330 CA, which is at the end of the liquid-spray event and the beginning of the spark discharge. The conditionally sampled averages discussed in Sect. 3.1 identified that the MF cycles are leaner and the velocities lower just downstream of the spark plug.

The contribution of the first POD mode of the equivalence ratio to the conditionally sampled reconstructed averages is nearly identical for the two samples as indicated by the nearly equal coefficients seen in Fig. 8. Thus, it is the modulations by the higher modes that create the differences in the ensemble averages by locally leaning or enriching the values given by the first mode. Figure 7 demonstrates that the impact of the modulations by modes 2–5 of the MFs is greater in magnitude and opposite in sign compared with the WB cycles. Inspection of the PDFs of the POD coefficients in Fig. 8 (conditionally sampled on WB and MF cycles) shows that the range of values of the mode 2 coefficients shows some separation between the WB and MF cycles, and that the MF values are larger. Almost all mode 2 coefficients for the MF cycles are positive; in the product with mode 2, this produces an overall negative contribution to the sum (Eq. 3) and thus, the addition of mode 2 makes almost every cycle is leaner. Although lower in magnitude, the same trends are seen for the PDFs and ε distributions of modes 3 and 6. Thus, the PDFs quantify the cycle-to-cycle variability of the modes. Also, the higher (lower energy) POD modes retain the structural information, lost in the Reynolds decomposition of the turbulence fluctuations.

The velocity distributions drive the changes in equivalence ratio distributions. Three major flow structures were identified in the ensemble mean distributions of Fig. 4 as well as the reconstructed flow fields. The energy spectra shown in Fig. 9 indicate that modes 2–20 in the MF conditionally sampled subset are more important than for the WB cycles. Indeed, the summation over the contributions from modes 2–20 has a pronounced effect on the reconstructed flow field. The dominant structure near the spark plug is the streaming structure (solid line circle, Fig. 11), presumed to be the wake (entrained air velocity) behind the liquid spray.

The vortex near the spark plug (dashed outline, Fig. 11) is presumed to be a result of the spray entrainment as well. This entrainment vortex appears in both conditionally sampled means (Fig. 4), but almost disappears when the means are subtracted. The POD analysis shows that this vortical structure exists only in modes 1 and 2 (Fig. 12), where the basis function rotates clockwise in mode 1 and counter clockwise in mode 2. In this case, the counter-rotating vortex in mode 2 is not a new structure, rather increases and decreases the magnitude of the same structure but by a small amount. The near-Gaussian PDF distribution of the WB POD mode 1 coefficients with a range of ±20 compared with an average value of around 68 for the mode 1 coefficient reveals a large cycle-to-cycle rotational variation. The MF PDF of mode 2 coefficients shows a negative bias, which coupled with the counter-rotating vortex in mode 2, reveals that mode 2 of the MF cycles tends to increase the energy of the entrainment vortex. However, the mode 1 coefficient is smaller for MF cycles (average of 58) so that overall the MF cycles have a weaker entrainment vortex. The cycle-to-cycle variability of this entrainment vortical structure is captured by the PDF of mode 2 but not apparent from the averaging analysis.

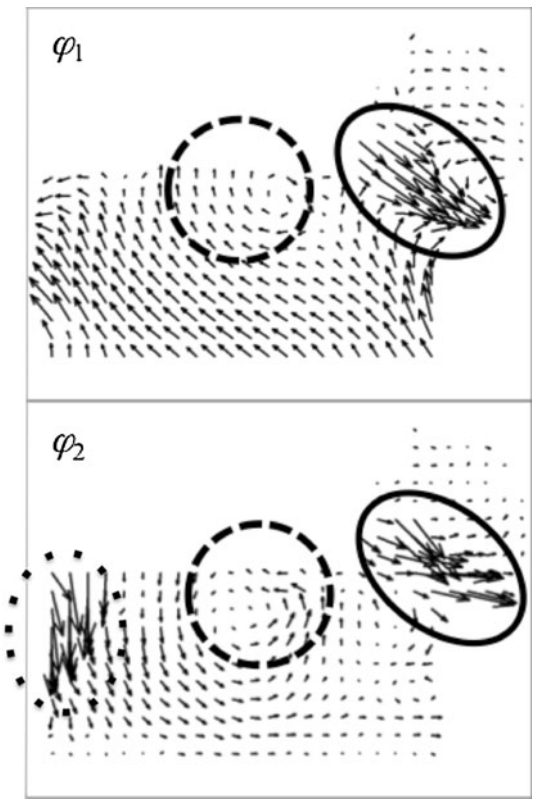

Fig. 12 Flow structures that are relevant to the study of misfires are composed from contributions in several modes. In particular, the regions highlighted by the outlines are discussed in the text

The vortical structure indicated by the dotted line (lower right panel in Fig. 11) is probably not of great importance to the region downstream of the spark plug and therefore to the success of ignition, but shows an important principle. It was not visible in either the WB or MF averages of Fig. 4 because it is superimposed on a spatially large and large-magnitude streaming structure. It becomes visible when subtracting the two averages because the streaming structure is dominant and captured primarily in mode 1 with little modulation by other modes. Thus, when the two means are subtracted, the superimposed vortical structure appears. In the POD analysis, this structure does not become very apparent until modes 2 through 20 are summed, though recognizable still not as distinct as in the subtracted means of Fig. 4. This is a case where POD has revealed a weak structure superimposed on a larger magnitude structure; also, it demonstrates that a single flow structure may be decomposed into many modes and thus requires many modes to reconstruct it.

4 Summary and conclusions

The merit of using proper orthogonal decomposition was explored for the analysis of conditions leading to rare failure in engine performance. Those conditions were previously identified in a high-speed imaging study by Peterson et al. (Peterson et al. 2011) for low-load late injection operation of a spray-guided direct injection engine. They used simultaneously acquired sequences of velocity and equivalence ratio images to identify that flow and mixture conditions in misfiring and partially burning cycles were such that an early flame kernel would develop too slowly and would be convected too slowly to eventually reach the main fuel cloud. The indicated mean effective pressure that was determined from in-cylinder pressure measurements provided information to differentiate globally the failing cycles (MF) from the well-burning cycles (WB) so that conditional sampling on the imaging could be performed. The present study analyzed the potential of using proper orthogonal decomposition and subsequent conditional sampling in revealing information that would not be accessible via conditionally sampled ensemble averaging.

As a baseline, the ensemble-averaged data, conditionally sampled on the WB and MF cycles, demonstrated clearly that the mixture was leaner and traveled at lower velocity in the wake region of the spray at the spark plug at the time of spark for MF cycles compared with WB cycles. However, interpretation of ensemble-average data in engines is often difficult because it is never certain if the observed structures are present in every cycle or the results of a few very energetic cycles.

Proper orthogonal decomposition was then performed on both velocity fields and equivalence ratio distributions. An initial analysis treating WB and MF data separately with POD yielded inconclusive results because modes and coefficients from the two decompositions could not be directly compared. POD of the combined data set of 200 WB and 37 MF images provided a common basis, i.e., set of modes, for further analysis that yielded the following observations.

1. The coefficients of each mode could be conditionally averaged to quantify the extent to which each mode contributes to the ensemble average distribution.
2. The PDFs of coefficients reveal the cycle-to-cycle variation of the structures and the extent of modulation of the first mode by higher modes.
3. The POD retains structural information on the turbulence fluctuations that is lost in Reynolds averaging.
4. The PDFs of coefficients from WB and MF cycles overlap, and therefore the identification of MF cycles solely from POD data is not possible but still requires additional information such as indicated mean effective pressure.

For both the velocity and equivalence ratio distributions, it was shown that the POD extracts the most energetic structures and modulates these structures (magnitude and, for velocity, direction) in the higher-order (lower energy) modes. However, it is crucial to note that the modes do not necessarily identify a real flow or mixture structure in a single mode; rather many modes may be necessary to reconstruct the structure.

Applying this approach to the misfire study data of Peterson et al. (2011), we conclude the following. The existence of the streaming structure associated with the wake of the liquid spray is in the first POD mode and has high energy in every cycle. This is expected, as the liquid spray momentum is much larger than that of the in-cylinder airflow. The modulation of this structure in the MF cycles occurs at higher order and requires many low-energy higher-order modes to reconstruct the flow field (cf. Fig. 11), suggesting significant spatial variation of the modulations. The POD modes of the equivalence ratio revealed that all of the lower-order modes contributed to leaning out of the mode 1 wake structure near the spark plug, which is the region where the spark-discharge plasma was convected (Peterson et al. 2011).

In summary, it was demonstrated that the application of proper orthogonal decomposition to velocity and equivalence ratio images was useful in identifying and analyzing the differences in flow and mixture conditions at the time of spark between well-burning and misfiring cycles. However, POD results alone were not sufficient to identify which of the cycles were misfiring cycles and additional information was required for conditional sampling.

Acknowledgments This work was supported by General Motors R&D within the GM-UM Collaborative Research Laboratory on Engine Systems Research at The University of Michigan. Hao Chen is grateful for financial support from Shanghai Jiao Tong University to enable a ten-month visit to the University of Michigan. Brian Peterson has provided the images on which this analysis is based on. The authors would also like to acknowledge discussions with Professor Min Xu and Yuyin Zhang from Shanghai Jiao Tong University. Finally, we are grateful for comments from an anonymous reviewer of ref. (Peterson et al. 2011) that inspired us to do the work presented here.

References

Baby X, Dupont A, Ahmed A, Deslandes W, Charnay G, Michard M (2002) A new methodology to analyze cycle-to-cycle aerodynamic variations. SAE 2002-01-2837

Bizon K, Continillo G, Leistner KC, Mancaruso E, Vaglieco BM (2009) POD-based analysis of cycle-to-cycle variations in an optically accessible diesel engine. Proc Combust Inst 32:2809–2816

Bizon K, Continillo G, Mancaruso E, Merola SS, Vaglieco BM (2010) POD-based analysis of combustion images in optically accessible engines. Combustion and Flame 157:632–640

Chatterjee A (2000) An introduction to the proper orthogonal decomposition. Curr Sci 78:808–817

Cordier L, Bergmann M (2003) Proper orthogonal decompsition: an overview lecture series 2003-04 in VKI, Post-processing of experimental and numerical data

Fajardo CM, Smith JD, Sick V (2006) Sustained simultaneous high-speed imaging of scalar and velocity fields using a single laser. Appl Phys B-Lasers Optics 85:25–30

Fansler T, Drake M, Böhm B (2008) High-speed Mie scattering diagnostics for spray-guided gasoline engine development 8th International symposium on internal combustion diagnostics. AVL, Baden–Baden, Germany

Fogleman M, Lumley J, Rempfer D, Haworth D (2004) Application of the proper orthogonal decomposition to datasets of internal combustion engine flows. J Turbulence 5

Holmes P, Lumley JL, Berkooz G (1996) Turbulence, coherent structures, dynamical systems and symmetry. Cambridge University Press, Cambridge

Holmes PJ, Lumley JL, Berkooz G, Mattingly JC, Wittenberg RW (1997) Low-dimensional models of coherent structures in turbulence. Phys Rep 287:337–384

Liu K, Haworth D (2011) Development and assessment of POD for analysis of turbulent flow in piston engines. SAE Paper 2011-01-0830

Lumley JL (1967) The structure of inhomogeneous turbulence. In: Yaglom AM, Tatarski VI (eds) Atmospheric turbulence and wave propagation, pp 166–178

Peterson B, Sick V (2009) Simultaneous flow field and fuel concentration imaging at 4.8 kHz in an operating engine. Appl Phys B 97:887–895

Peterson B, Reuss DL, Sick V (2011) High-speed imaging analysis of misfires in a spray-guided direct injection engine. Proc Combust Inst 33:3089–3096

Roudnitzky S, Druault P, Guibert P (2006) Proper orthogonal decomposition of in-cylinder engine flow into mean component, coherent structures and random Gaussian fluctuations. J Turbulence 7:1–19

Sick V, Drake MC, Fansler TD (2010a) High-speed imaging for direct-injection gasoline engine research and development. Exp Fluids 49:937–947

Sick V, Reuss D, Rutland C, Haworth D, Oefelein J, Janicka J, Kuo T-W, Freitag XY (2010b) A common engine platform for engine LES development and validation. In: Angelberger C (ed) LES4ICE. IFP Energies Nouvelles, Rueil-Malmaison, France

Sirovich L (1987) Turbulence and the dynamics of Coherent structures.1. Coherent structures. Q Appl Math 45:561–571

Sirovich L, Kirby M (1987) Low-dimensional procedure for the characterization of human faces. JOSA A 4:519–524

Voisine M, Thomas L, Boree J, Rey P (2011) Spatio-temporal structure and cycle to cycle variations of an in-cylinder tumbling flow. Exp Fluids 50:1393–1407

Zhao F, Lai M-C, Harrington DL (1999) Automotive spark-ignited direct-injection gasoline engines. Prog Energy Combustion Sci 25:437–562